

# Seeing Double: Indications From *TESS* and *Gaia* That PTFO 8-8695b is Not a Planet

L. G. BOUMA<sup>1</sup> AND J. N. WINN<sup>1</sup>

<sup>1</sup> *Department of Astrophysical Sciences, Princeton University, 4 Ivy Lane, Princeton, NJ 08540, USA*

(Received April 17, 2020; Revised —; Accepted —)

Submitted to AAS journals.

## ABSTRACT

PTFO 8-8695b is a candidate hot Jupiter in the 7–10 million year old Orion-OB1a cluster. We inspected data from *TESS* and *Gaia* to clarify whether it is actually a planet. The *TESS* lightcurve shows that the dominant variability in this system is a sinusoid with a “long” period  $P_\ell = 11.96$  hr, likely caused by stellar rotation. Also present is a complex signal, previously identified as the planet candidate, that repeats with a “short” period  $P_s = 10.74$  hr. The two signals beat every 4.48 days. Although there is a dip in the short-period signal, ground-based photometry from the past decade shows that the orbital phase of the dip seems to have instantaneously jumped, at least once, and perhaps twice. Planets do not “jump” in orbital phase. Furthermore, the *Gaia* data show that PTFO 8-8695 is probably a photometric binary. Given the evidence, we believe that PTFO 8-8695 is a binary M dwarf in which one star shows the “long” rotation signal, and the other is showing “transient dipping” that has also been observed in other young M dwarfs. The planetary interpretation seems unlikely.

**Keywords:** Exoplanet evolution (491), Open star clusters (1160), Stellar ages (1581), Stellar rotation (1629), Variable stars (1761)

## 1. INTRODUCTION

If PTFO 8-8695b were a planet, it would be exceptional. Transiting a sub-10 Myr old weak-lined T Tauri M dwarf in Orion, it would be the youngest hot Jupiter known (van Eyken et al. 2012). Its orbital period of only 10.7 hours would also give it the shortest period of any known hot Jupiter. With such a short period, it would almost certainly have filled its Roche lobe, and would be actively losing mass to its host star. Not only that, but the rapidly rotating host star would also be oblate and gravity darkened, and so the planet’s orbit would likely precess into and out of transitability (Barnes et al. 2013; Ciardi et al. 2015; Kamiaka et al. 2015).

Other lines of evidence would imply further planetary “firsts” for this planet candidate. One first would be that its transits are about three times deeper in optical bandpasses (e.g., *g*-band) than in the near-infrared (e.g., *z*-band) (Onitsuka et al. 2017; Tanimoto et al. 2020). A cloud-free hydrogen-dominated planetary atmosphere cannot explain such a wavelength dependence. The planet might therefore be surrounded by a dust cloud (Tanimoto et al. 2020).

Another first could be the direct detection of  $H\alpha$  emission from the planet itself (Johns-Krull et al. 2016). While the

stellar chromosphere emits in  $H\alpha$ , it seems that there is an additional excess  $H\alpha$  emission that could be in phase with the planetary orbit. The average velocity width of the excess  $H\alpha$  emission is  $87 \text{ km s}^{-1}$ , and its equivalent width is 70–80% that of the stellar chromosphere (Johns-Krull et al. 2016). The proposed explanation is that the outflowing mass from the planet may explain this excess emission as well (Johns-Krull et al. 2016).

There are perhaps a few challenges to the planetary interpretation (if these “features” are not already seen as such). They include that the planet does not seem to emit infrared radiation in occultation, at least anywhere near the expected amplitude (Yu et al. 2015). In addition, despite measurement attempts by multiple investigators, it does not seem to show the Rossiter effect at the amplitude expected given the rapid stellar rotation and large planet size (Yu et al. 2015; Ciardi et al. 2015). Finally, detailed modelling of the “precession + gravity darkening” transits has shown that the necessary degree of gravity darkening is too great, given the spectroscopically observed equatorial velocity (Howarth 2016). Additionally, as the gravity-darkened star precessed about its rotation axis, it would need to show photometric variability that has not been observed.

While the planetary interpretation has challenges, alternative explanations do as well. High-latitude accretion hotspots might produce the observed  $H\alpha$  variability, but PTFO 8-8695 does not have an infrared (IR) excess associated with the presence of an inner disk. Low-latitude starspots, hot or cold,

struggle to produce the necessary dip durations. A circumstellar cloud of dust or gas might be entrained in the stellar magnetosphere, but clumps would need to be invoked to explain the short-duration flux dips.

In the following, Section 2 presents newly available observations from the Transiting Exoplanet Survey Satellite (TESS; [Ricker et al. 2015](#)) and Gaia ([Gaia Collaboration et al. 2018](#)). Analyzing the TESS data in Section 3, we find two distinct signals. A long sinusoid repeats every 12.0 hours, and is probably stellar rotation. A short “dip + complex modulation” repeats every 10.7 hours. Analyzing the Gaia data in Section 4, we show that PTFO8-8695 is quite likely a photometric binary. In Section 5, we note that the orbital phase of the dip seems to have instantaneously changed, perhaps twice. We argue that PTFO8-8695 is a binary M dwarf in which one star shows a rotation signal, and the other is showing “transient dipping” that has been observed in other young M dwarfs, and is likely caused by eclipses of warm particulate clouds. Section 7 summarizes our main points.

## 2. THE DATA

### 2.1. TESS Observations

PTFO8-8695 was observed by TESS with Camera 1, CCD 1, from December 15, 2018 to January 6, 2019, during the sixth sector of science operations ([Ricker et al. 2015](#)). The star was designated TIC 264461976 in the TESS Input Catalog ([Stassun et al. 2018, 2019](#)). The pixel data for an  $11 \times 11$  array surrounding PTFO8-8695 were averaged into 2-minute stacks by the onboard computer. Each  $2048 \times 2048$  image from the CCD was also averaged into 30-minute stacks, and saved as a “full frame image” (FFI).

The 2-minute stacks for PTFO8-8695 were then reduced to lightcurves by the Science Processing Operations Center (SPOC) at NASA Ames ([Jenkins et al. 2016](#)). Our main analysis used the resulting Presearch Data Conditioning (PDC) lightcurve. The PDC lightcurve aperture used pixels chosen to maximize the SNR of the total flux of the target ([Smith et al. 2017a](#)). Non-astrophysical variability was removed through the methods discussed by [Smith et al. \(2017b\)](#).

As an independent check on the shorter cadence SPOC light-curve, we separately processed the 30-minute image stacks as part of the Cluster Difference Imaging Photometric Survey (CDIPS; [Bouma et al. 2019](#)). The CDIPS lightcurve used a circular aperture with radius 1 pixel.

To clean the data, we removed all points with non-zero quality flags (*e.g.*, [Tenenbaum & Jenkins 2018](#)). We also masked out the first and last 6 hours of each orbit, since there is often systematic red noise during those times. Both the CDIPS and PDC lightcurves showed a clear discontinuous “jump” in the last few days of orbit 20, which seemed likely to be an instrumental systematic. We correspondingly masked out times from BJD 2458488.3 until the end of the orbit. The PDC lightcurve initially had 15,678 points. The quality cut removed 854 points, masking the orbit edges removed an additional 716, and removing the final few days of

orbit 20 removed an additional 1079. After cleaning, 83% of the initial flux measurements remained.

We normalized these points by dividing out the median flux. We then subtracted by unity to simplify subsequent analysis. Many of these and subsequent processing steps were performed using `astrobase` ([Bhatti et al. 2018](#)).

### 2.2. Gaia Observations

Between July 25, 2014 and May 23, 2016, Gaia acquired 121 “good” observations of PTFO8-8695, *i.e.*, observations that were not strongly downweighted in the astrometric solution of the source (CITE). The Gaia data processing team at XXXINSTITUTION combined the XXX and YYY into a global astrometric solution, from which the parallax of PTFO8-8695 was derived (CITE). The star was assigned a Gaia DR2 identifier of 3222255959210123904 (CITE). In addition, measurements of the stellar proper motion between observation epochs were made.

One point of note: Gaia DR2 measured a significant “astrometric excess”, at a level of  $10.3\sigma$ . This astrometric excess indicates the degree to which a single-source model fails to explain the observed astrometric measurements (CITE).

### 2.3. Cluster Membership

The Orion molecular cloud complex has numerous subgroups, with ages spanning 1 to 15 Myr (CITE). PTFO8-8695 has been known to be a member of the Orion OB1a association since at least CITE (Briceno 2005). Its relation to the broader Orion complex has been further explored by CITE<sub>X</sub>, CITE<sub>Y</sub>, and CITE<sub>Z</sub> (Briceno 05, 08, 18, whomever Van Eyken cites, and Kounkel 18).

In describing the cluster membership of PTFO8-8695, we follow the notation and results of [Kounkel et al. \(2018\)](#). [Kounkel et al. \(2018\)](#) combined astrometric data from Gaia DR2 with spectroscopic data from APOGEE-2 (CITE). They then performed a hierarchical clustering on the six dimensional position and velocity information to identify subgroups within the Orion complex. From smallest to largest groups, PTFO8-8695 was identified as being a member of the following nested subgroups:

$$25\text{Ori-1} \subset 25\text{Ori} \subset \text{Orion OB1a} \subset \text{Orion D}, \quad (1)$$

where from set-notation, ‘ $\subset$ ’ denotes “is a proper subset of”.

While all members of the Orion complex are young relative to the field, the internal age dispersion between different subgroups is measurable. The Orion Nebula Cluster (M42) is a site of ongoing star-formation, and its stars are 1-3 Myr old (CITE). 25 Ori1, by contrast, is XX-XX Myr old (CITE). These details are essential when assessing any evidence for photometric binarity in PTFO8-8695, because there is a degeneracy between stellar luminosity and age for stars on the pre-main-sequence. Having a clean sample of tightly spatially and kinematically associated stars is essential to minimize contamination not just from the field, but from older and younger members of the Orion complex itself.

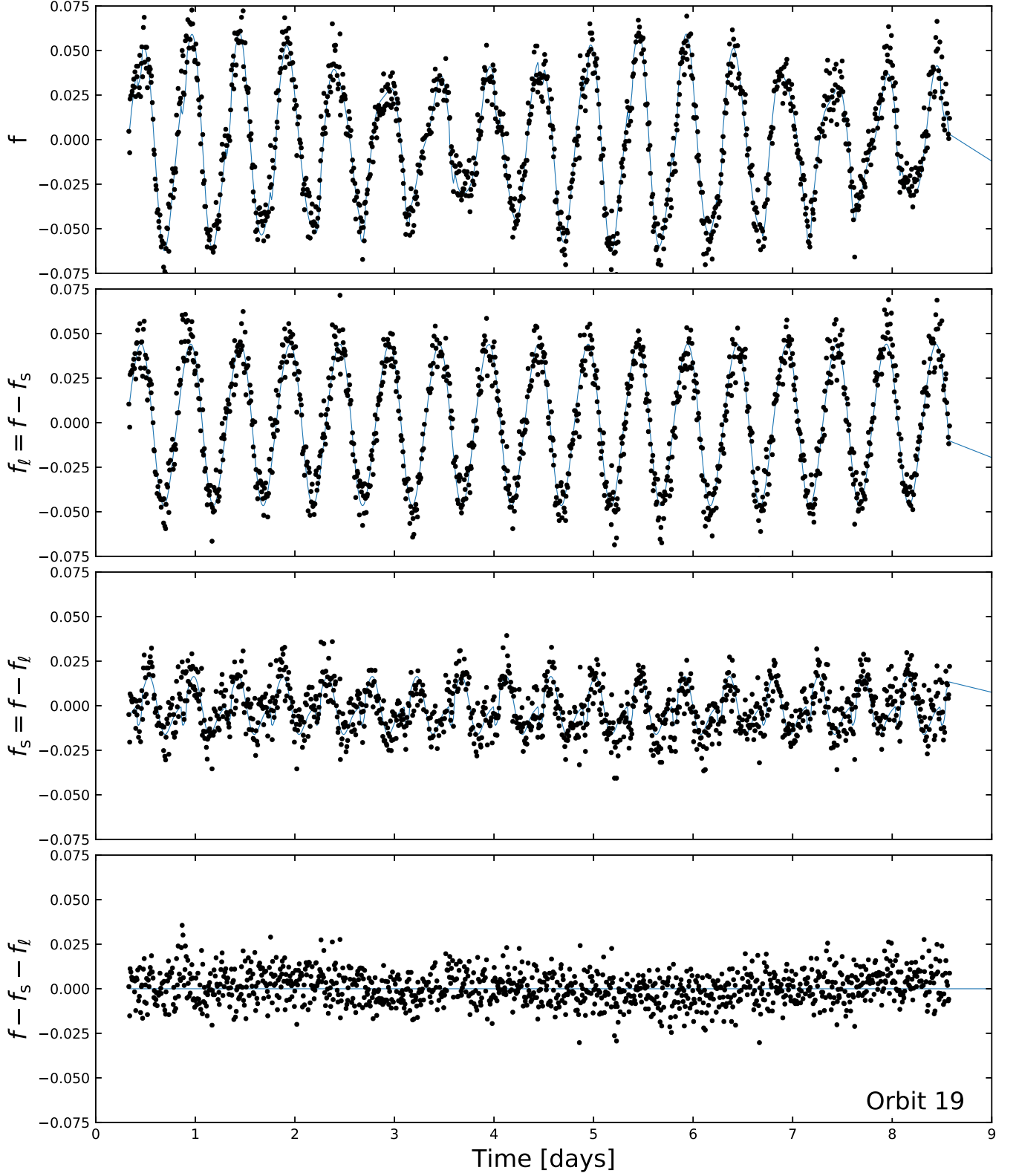


**Figure 1.** TESS lightcurve of PTFO 8-8695 (Sector 6, Orbit 19). *Top*: “Raw” PDCSAP mean-subtracted relative flux versus time. The beat period of 4.48 days is visible by eye. The preferred model plotted underneath the data includes 2 harmonics at the long period  $P_\ell$ , plus 2 harmonics and a transit at the short period  $P_s$ . *Upper middle*: Long-period signal, equal to the raw signal minus the short-period signal. *Lower middle*: Short-period signal, equal to the raw signal minus the long-period signal. *Bottom*: residual. The data are binned from 2 to 10 minute cadence as a convenience for plotting and fitting.

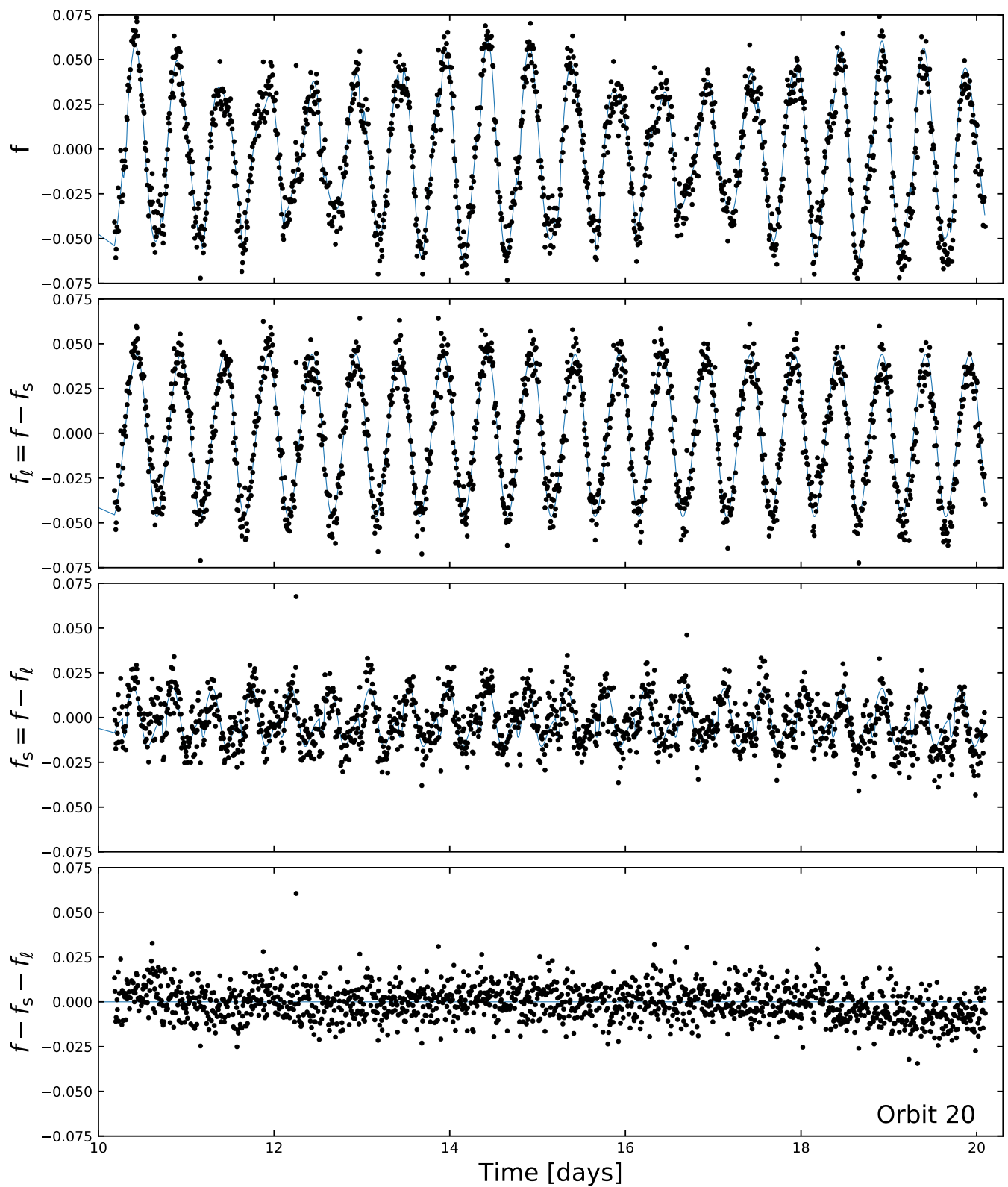
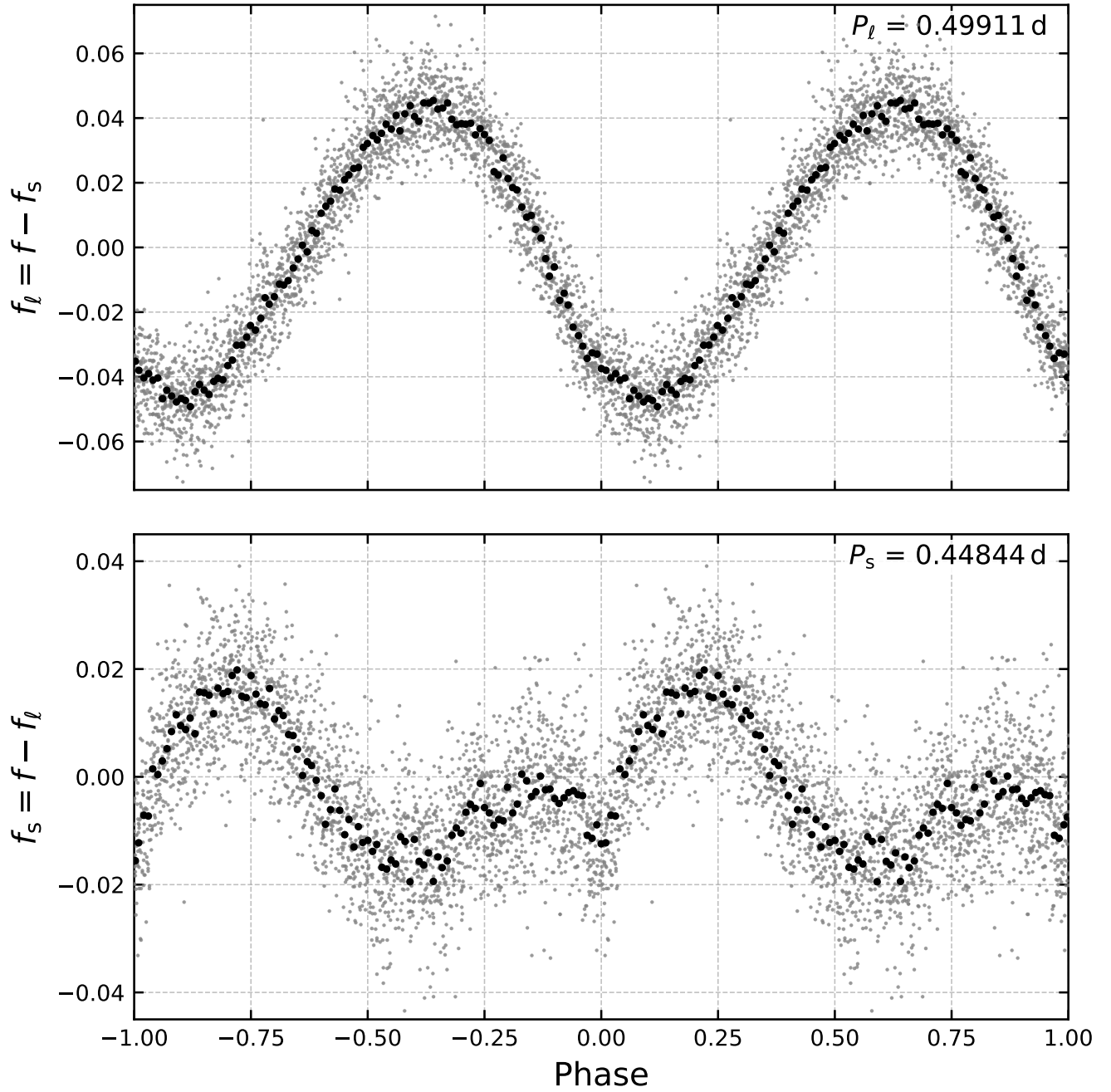


Figure 2. TESS lightcurve of PTFO8-8695 (Sector 6, Orbit 20). Panels are as in Figure 1.



**Figure 3. Phase-folded long and short-period signals.** *Top:* Long-period signal, as in Figure 1. *Bottom:* Short-period signal. The reference phase is set to the “planetary” dip. Gray points are the 10 minute cadence PDCSAP flux. Black points are binned to 100 points per period.



### 3. TESS ANALYSIS

#### 3.1. Inspection

Our initial inspection of the lightcurve, in both its 2-minute PDCSAP and 30-minute FFI forms, showed a strong sinusoidal beat signal (Figure 1, top panel).

As a precursor to more detailed analysis, we calculated generalized Lomb-Scargle periodograms using *astrobase* (Lomb 1976; Scargle 1982; VanderPlas & Ivezić 2015; Bhatti et al. 2018). The two largest peaks in the Lomb-Scargle periodogram of the lightcurve were clearly separated at a “short” period  $P_s \approx 0.448$  days and a “long” period  $P_\ell \approx 0.499$  days. The  $P_\ell$  peak had the greater power of the two. Smaller harmonics from each of these two dominants peaks were also present.

The peak-to-peak amplitude at maximum, when the two signals constructively interfere, is about 14%. At minimum, the peak-to-peak amplitude is about 6%. Assuming the signals are just two sinusoids, algebra tells us that the peak-to-peak amplitudes should therefore be 10% for the long-period signal, and 4% for the short-period signal. These order-of-magnitude numbers will turn out to be roughly correct.

Initial signal-processing experiments fitting out splines or sinusoids showed that after subtracting out the long-period signal, the short-period signal dominated the periodogram, and vice-versa. However it quickly became clear that it would be beneficial to simultaneously model the signals separately, in order to preserve the power at each frequency.

#### 3.2. Lightcurve Model

We opted to model the lightcurve as a linear combination of Fourier harmonics at the short and long periods, plus a transit at the short period. Symbolically, the total flux  $f$  is given as

$$f = f_s + f_\ell = f_{\text{transit},s} + f_{\text{Fourier},s} + f_{\text{Fourier},\ell}, \quad (2)$$

where  $f_s$  is the relative flux at the short period, and  $f_\ell$  is the flux at the long period. Writing out the Fourier terms,

$$f = f_{\text{transit},s} + \sum_{n=1}^N A_n \sin(n\omega_s t) + \sum_{n=1}^N B_n \cos(n\omega_s t) + \sum_{m=1}^M A_m \sin(m[\omega_\ell t + \phi_\ell]) + \sum_{m=1}^M B_m \cos(m[\omega_\ell t + \phi_\ell]), \quad (3)$$

for  $N$  and  $M$  the total number of harmonics at the short and long periods, respectively,  $A_i$  and  $B_i$  the amplitudes for each harmonic term (potentially negative), and  $\omega_i = 2\pi/P_i$  the angular frequency for  $i$  the short or long period index. We fixed the “phase-offset” for the short period signal to be zero, and let the reference time for the long period signal float by introducing  $\phi_\ell$ . Since we did not a priori know how many harmonics would be appropriate, we considered a number of different choices for  $N$  and  $M$ , and used the Bayesian information criterion to choose the appropriate model (Table 1).

As an example, one possible model could be a transit, plus  $N = 2$  harmonics of sines and cosines at the short period, plus

$M = 1$  harmonics at the long period. In this case, the free parameters would be as follows. For the transit, we would fit for the impact parameter, the planet-to-star radius ratio, two quadratic limb darkening parameters, the planet orbital period (equal to the short period), the reference time for the transit, and the mean flux. There would be  $2N = 4$  additional Fourier amplitudes at the short period, plus  $2M = 2$  Fourier amplitudes at the long period, and well as the long period itself and its phase. For this case, we therefore fitted 14 free parameters.

We implemented and fitted the models using *PyMC3*, which is built on *theano* (Salvatier et al. 2016; Theano Development Team 2016). For the Fourier terms, we used the default math operators. For the exoplanet transit, we used the model and derivatives implemented in *exoplanet* (Foreman-Mackey et al. 2020). Our priors are listed in Table 7. To speed up the fitting, we binned the cleaned 2 minute lightcurves to 10 minute bins. We correspondingly scaled the uncertainties in the flux measurements by a factor of  $\sqrt{5}$ . Before sampling, we initialized each model to the maximum a posteriori (MAP) solution. We then sampled using *PyMC3*’s gradient-based No-U-Turn Sampler (Hoffman & Gelman 2014), and used  $\hat{R}$  as our convergence diagnostic (Gelman & Rubin 1992). We tested our ability to successfully recover injected parameters using synthetic data, before switching to the actual PTFO8-8695 lightcurves.

#### 3.3. Fitting Results

We considered nine models, with the number of harmonics per frequency  $N$  and  $M$  ranging from one to three. To select our preferred model, we used the Bayesian information criterion (Table 1). The model with the lowest BIC had two harmonics at the short 10.74 hr period, and two harmonics at the long 11.96 hr period. All of the models have reduced  $\chi^2$  ranging between 1.37 and 1.51, which suggests a plausible though imperfect agreement between the data and models.

To explore where each model succeeded and failed, we split the raw signal into its respective components (Figures 1 and 2). We also examined the phase-folded signals (Figure 3).

In every model, the variability at the long period is a simple sinusoid with peak-to-peak amplitude  $\approx 10\%$ . The variability at the short period is always more complex. A dip of depth  $\approx 1.2\%$ , fit in our model as a transit, lasts  $\approx 0.75$  hours. Superposed on the dip is a complex signal with peak-to-peak amplitude of about 4%, which peaks near phase 0.25, and reaches minimum brightness between phases -0.5 and -0.25.

Outside of the primary dip, the short-period signal is relatively smooth, at least from phases 0 to 0.5. However the short-period signal is asymmetric. The flux from phases -0.5 to 0 shows what could be a discontinuous jump, shortly after reaching minimum. This jump was visible in each of the nine models we considered.

The periodogram of the final residual (Figure 1 bottom row) shows a weakly significant, poorly resolved peak at  $\approx 8$  days, consistent with the visual impression in the time domain that there could be a weak long-period signal present.

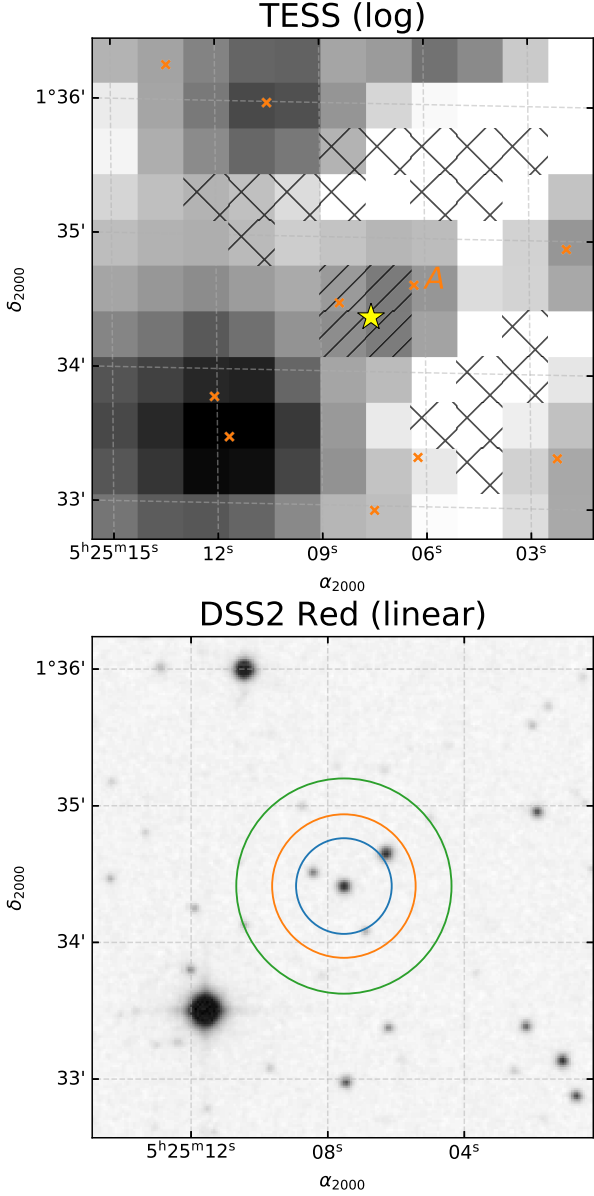


**Figure 4. Scene used for blend analysis.** *Top:* Mean TESS image of PTFO 8-8695 over Sector 6, with a log-stretch. The position of PTFO 8-8695 is shown with a yellow star. Neighbors with  $T < 17$  are shown with orange crosses. The apertures used to measure the background and target star flux are shown with  $\times$  and  $/$  hatches, respectively. *Bottom:* Digitized Sky Survey  $R$ -band image of the same field, with a linear stretch. The circles show apertures of radii 1, 1.5, and 2.25 pixels used in part of our blend analysis. The pixel level TESS data show that “Star A” does not contribute variability at either of the two observed periods (see Section 3.4).

### 3.4. Blend considerations

The TESS pixels are  $\approx 21''$  per side, and so before making an interpretation, we need to consider whether light from neighboring stars could have affected the photometry. The scene is shown in Figure 4. The pixels used to measure the

background level in the SPOC lightcurve are indicated with an ‘ $\times$ ’ hatch, and the pixels used in the final lightcurve aperture are shown with the ‘ $/$ ’ hatch.

The target star, PTFO 8-8695 (TIC 264461976), has a  $T$ -band magnitude of 14.0, and its position is shown with a star. The other (unlabeled) star inside the target aperture, TIC 264461979, has  $T = 16.8$  and so cannot contribute a signal with relative amplitude 10%. The only neighbor that is sufficiently close and bright that its light might contaminate the target star is TIC 264461980, with  $T = 14.8$ , which we denote “Star A”. Star A is  $23.6''$  NW of our target, and based on the magnitude difference could contribute up to 48% the flux of our target star, PTFO 8-8695.

Because PTFO 8-8695 has previously been identified to have periodicity consistent with our measurement of  $P_s$ , our main concern regarding blending is the degree to which we can be certain that the long-period signal at  $P_\ell$  also originates from PTFO 8-8695. We took two approaches towards determining the source of the long-period signal.

First, we examined the CDIPS full frame image lightcurves of the target, which are available on MAST (Bouma et al. 2019). The maximal peak-to-peak beat amplitude is consistently  $\approx 10\%$  across apertures of radii 1, 1.5, and 2.25 pixels. If Star A were the source of the long-period variability, we would expect the peak variability amplitude to be smallest in the 1 pixel aperture, based on the separation of the sources (Figure 4, bottom). From this test alone, it seems unlikely that Star A is the source of the long-period signal.

Second, we examined the lightcurve of each pixel in the scene individually. We opted to use the interactive tools implemented in `lightkurve` (Lightkurve Collaboration et al. 2018). If Star A were the source of the long-period variability, we would expect the pixels nearest to Star A to show a sinusoidal signal with amplitude exceeding 10%. We find no evidence for this being the case. The pixel directly below Star A does not clearly show the sinusoidal variability, and the peak-to-peak variability in that pixel is  $\lesssim 8\%$ . In contrast, the south-easternmost pixel within PTFO 8-8695’s aperture (the pixel furthest from Star A that was used in the optimal aperture) shows the  $P_\ell$  sinusoidal variability signal at  $\approx 10\%$  amplitude.

As there is no evidence in favor of a blend scenario, we conclude that both the  $P_s$  and  $P_\ell$  signals originate from PTFO 8-8695, at least within the resolution of the Gaia-DR2 source catalog. However, as we shall see, PTFO 8-8695 itself could still be a binary.

## 4. GAIA ANALYSIS & PHOTOMETRIC BINARITY

Schmidt et al. (2016) Lee & Chiang (2018)

To assess the cluster membership and potential binarity of PTFO 8-8695, we needed to identify stars with which it was and was not coeval. The simplest way to do this—clustering based on six-dimensional position and kinematic information—had already been done by Kounkel et al. (2018). For simplicity, we considered the members they identified brighter than  $G_{\text{RP}}$  of 16. This yielded 149 stars in 25 Ori-1, mostly M dwarfs. Kounkel et al. (2018) identified

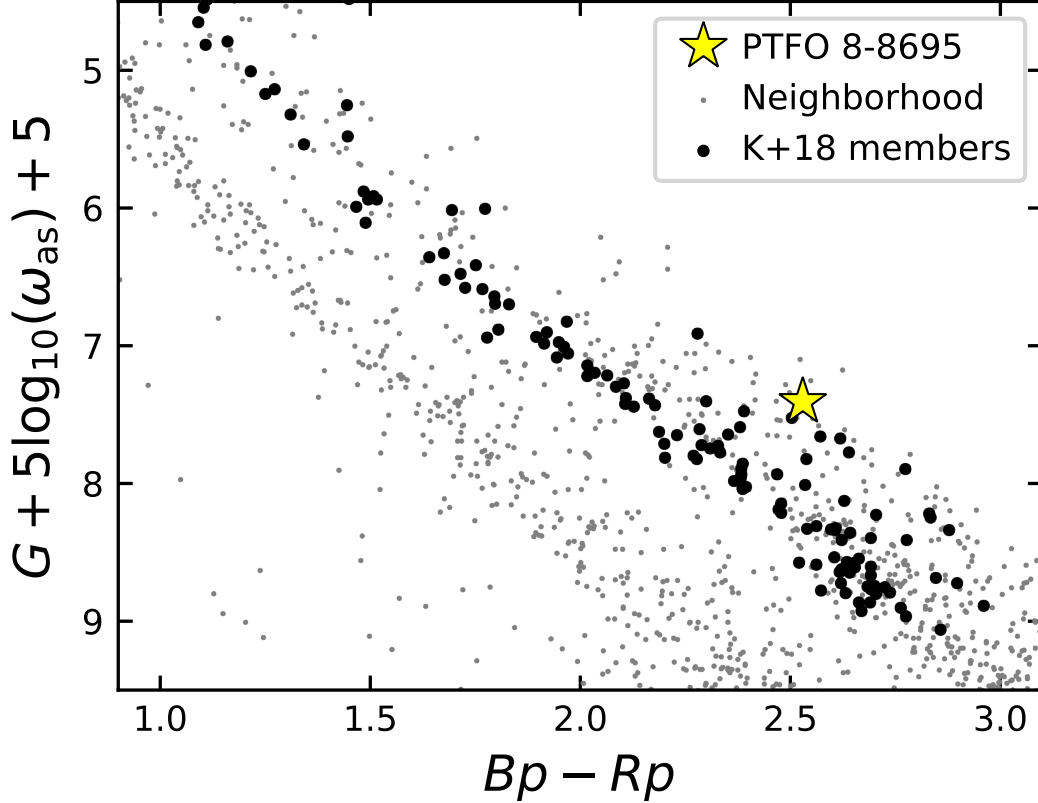


**Figure 5. Hertzsprung-Russell diagram of PTFO 8-8695 and late-type members of 25 Ori-1.** Members of the 25 Ori-1 group (black circles) were identified by Kounkel et al. (2018) through clustering on six-dimensional Gaia-DR2 and APOGEE-2 data. The reference “neighborhood” (gray circles) is the group of at most  $10^4$  randomly selected non-member stars within 5 standard deviations of the mean 25 Ori-1 right ascension, declination, and parallax. It contains members of the full Orion complex with a wider spread of ages, in addition to field interlopers.  $G$  is the Gaia broadband,  $Bp$  is Gaia blue,  $Rp$  is Gaia red, and  $\omega_{\text{as}}$  is the parallax in arcseconds. The  $x$ -axis limits have been set to show only K and M dwarf members, to accentuate PTFO 8-8695’s separation from the single-star sequence.

seven other smaller groups in the Orion complex near the Be star 25 Ori. These groups received higher numbers, *e.g.*, 25 Ori-2.

To define a set of non-member stars that nonetheless had comparable selection functions, we defined a reference “neighborhood” as the group of at most  $10^4$  randomly selected non-member stars within 5 standard deviations of the mean 25 Ori-1 right ascension, declination, and parallax. We queried these stars using the `astroquery` package, which provides a convenient interface to the Gaia archive (CITE, CITE). This yielded 1,819 neighbors. While some of these stars may indeed be members of the Orion complex, or even of 25 Ori-1, enforcing this cut on positions and parallaxes ensures that we are querying stars with comparable amounts of interstellar reddening.

We examined the resulting five-dimensional right ascension, declination, proper motions, and parallaxes. The first point we noted was that 25 Ori-1 was a clearly defined overdensity in each dimension, so the cluster exists, and is different from the neighborhood. PTFO 8-8695 was also clearly a member in each of these projected dimensions.

Given our detection of two separate signals, whether PTFO 8-8695 could be a photometric binary was of great interest. Figure 5 shows the HR diagram from which we assessed this issue. The diagram shows that PTFO 8-8695 is  $\approx 0.8$  magnitudes brighter than the average 25 Ori-1 star of the same color. In other words, it is about twice as bright. It also seems to be on the photometric binary track of the cluster, which has a few other stars.

The implication is that either (i) PTFO 8-8695 is notably younger than the kinematically identical cluster members, or (ii) PTFO 8-8695 is a photometric binary. Given the independent presence of two resolved signals, we favor the interpretation that PTFO 8-8695 is a binary star system.

## 5. DISCUSSION

### 5.1. Long period sinusoid

The standard interpretation of sinusoidal modulations for a pre-main-sequence M dwarf is that we are observing a stellar rotation period of 11.96 hours. This is the dominant signal in the system with 10% amplitude, and there is no evidence to suggest that this signal has any other origin.



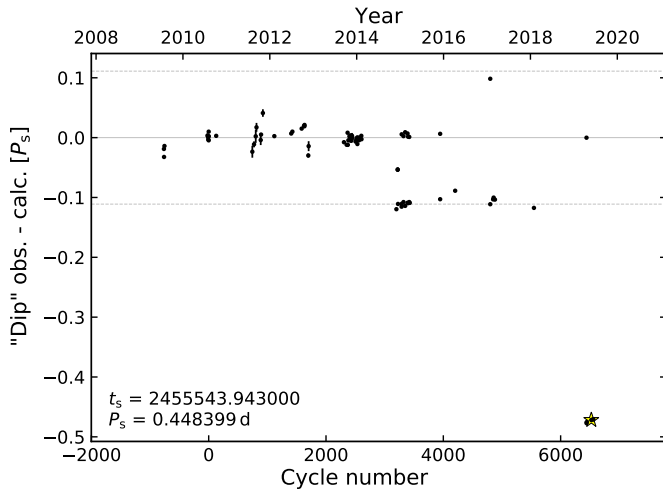


**Figure 6. Timing residuals for PTFO 8-8695b from a decade of monitoring.** Black points are times of “dips”, minus the indicated linear ephemeris. The y-axis is given in units of phase for the short-period signal. The star shows the binned TESS ephemeris. “Dips” have been observed by [van Eyken et al. \(2012\)](#), [Ciardi et al. \(2015\)](#), [Yu et al. \(2015\)](#), [Raetz et al. \(2016\)](#), [Onitsuka et al. \(2017\)](#), and [Tanimoto et al. \(2020\)](#). Certain dips (*e.g.*, the one at phase 0 in mid-2019) are consistent with noise, and were likely reported because something was *expected*, rather than convincingly *observed*. Horizontal dashed lines are drawn at  $\pm(P_l - P_s)/P_s$ , highlighting a possible observational bias. The orbital phase observed by TESS is consistent with that of [Tanimoto et al. \(2020\)](#), and quite different from the original phase.

The discovery study by [van Eyken et al. \(2012\)](#) saw the same signal (*e.g.*, their Figure 7), but identified its alias as a periodogram peak at  $0.9985 \pm 0.0061$  days. They ascribed it to their observing cadence, because of its close correspondence to the sidereal day. While the TESS data can show significant reflected light from the Earth (*e.g.*, [Luger et al. 2019](#)), our pixel-level analysis showed that the signal is specific to only pixels near PTFO 8-8695, and no other pixels. We therefore conclude that the signal is not a systematic.

We are not the first to reach the conclusion that the long period sinusoidal modulation is astrophysical. A follow-up study by [Koen \(2015\)](#) identified the same modes and aliases as [van Eyken et al. \(2012\)](#), but argued that the 0.50 d signal was astrophysical. Using archival photometry and photometry from the YETI global telescope network, [Raetz et al. \(2016\)](#) eventually came to the conclusion that the 0.50 d signal was indeed from stellar rotation. The TESS data strongly support this conclusion.

### 5.2. Short period dip

The dip lasts about 45 minutes, and seems to re-occur every 10.74 hours (Figures 1, 2, 3). The dip duration is roughly the same as that observed by previous investigators ([van Eyken et al. 2012](#); [Yu et al. 2015](#)). The dip depth is comparable to what has been observed in red visual bands...

*Epoch*—The TESS dip does not phase up where it is supposed to... Figure 6

### 5.3. Short period out-of-dip modulation

If there were a giant planet transiting PTFO 8-8695, it would tidally distort the host star, and cause ellipsoidal photometric modulations. The amplitude of the ellipsoidal distortion for a  $1 M_{\text{Jup}}$  companion would be about 1400 ppm ([Shporer 2017](#)). This is significantly larger than the typical ellipsoidal modulation induced by close-in giant planets because the host star is puffy, and still on the pre-main-sequence. For our estimate, we assumed  $R_* = 1.39 R_{\odot}$ , and  $M_* = 0.39 M_{\odot}$  ([van Eyken et al. 2012](#)).

Our preferred model does detect a significant ellipsoidal signal, parametrized as the “ $B_1$ ” component. The amplitude of the signal is  $0.53 \pm 0.06\%$ . Interpreted as being caused by a planet, it would imply a minimum planet mass  $M_p \sin i$  of  $3.8 M_{\text{Jup}}$ .

## 6. PHYSICAL INTERPRETATION

Given the evidence, we believe that PTFO 8-8695 is a binary M dwarf in which one star shows the “long” rotation signal, and the other is showing “transient dipping” that has also been observed in other young M dwarfs.

Many other young M-dwarf photometric binaries have been observed in *e.g.*, Upper Sco and the Pleiades to show multiple periods ([Rebull et al. 2018](#); [Stauffer et al. 2018](#)). Typically, the periods are both rotational modulation.

However, occasionally one or both periods can be “scallop-shell” variability, *e.g.*, EPIC 203956650 in  $\rho$ Oph ([Rebull et al. 2018](#)).

There are

The gas in the disks is gone (CITE). The upper limits on the SED from [Yu et al. \(2015\)](#) imply X, Y, Z. The stars are therefore presumably no longer “magnetically locked” to their disks. This is consistent with the  $\approx$ half-day periodicities of both signals. In the broader context of rapidly rotating young M-dwarfs, “magnetic locking” causes classical disked T-Tauri stars tend to rotate more *slowly*, and almost none have periods less than two days (*e.g.*, [Rebull et al. 2020](#)).

The main physical question is what is causing the “transient dipping”. This is an unsolved problem not only for PTFO 8-8695 but also for an entire class of young rapidly rotating M-dwarfs

The roughly half-day periods of both signals imply that

## 7. CONCLUSIONS

PTFO 8-8695 was previously thought to potentially host a hot Jupiter. The TESS lightcurve of PTFO 8-8695 showed a number of new features, many of which seem to disfavor the hot Jupiter interpretation. The TESS data showed two key pieces of evidence.

1. *Two periodic signals.* The “long” signal is a 10% peak-to-peak sinusoidal modulation repeating every 11.96 hours. The “short” signal is a 4% peak-to-peak complex modulation repeating every 10.74 hours. It is

composed of a dip, plus at least two harmonics. The signals beat, and therefore cannot be an artifact linked to data processing.

2. *A dip at the wrong orbital phase.* The clearest dip in the “short” signal was consistent with recent observations by [Tanimoto et al. \(2020\)](#), and differed from the discovery epoch by 5.14 hours.

The physical mechanism responsible for all these features remains a matter of speculation. With that said, the TESS data support new arguments against the planetary interpretation of PTFO 8-8695. First, if the long signal is caused by starspot modulation, and the short signal by a transiting planet, what causes the additional complex modulations seen at the short, “orbital”, period?

Similarly, if the planet truly orbits every 10.74 hours, while the star’s equator spins every 11.96 hours, the situation is clearly Darwin unstable.

Given the available evidence, PTFO 8-8695 seems consistent with the “transient dipping” phenomenology observed in many young M dwarfs. It seems rather unlikely to be a planet.

*Software:* `astrobase` ([Bhatti et al. 2018](#)), `astropy` ([Astropy Collaboration et al. 2018](#)), `astroquery` ([Ginsburg et al. 2018](#)), `corner` ([Foreman-Mackey 2016](#)), `exoplanet` ([Agol et al. 2019](#)) `exoplanet` ([Foreman-Mackey et al. 2020](#)), and its dependencies ([Agol et al. 2019](#); [Kipping 2013](#); [Luger et al. 2019](#); [Theano Development Team 2016](#)). `IPython` ([Pérez & Granger 2007](#)), `lightkurve` ([Lightkurve Collaboration et al. 2018](#)), `matplotlib` ([Hunter 2007](#)), `MESA` ([Paxton et al. 2011, 2013, 2015](#)) `numpy` ([Walt et al. 2011](#)), `pandas` ([McKinney 2010](#)), `PyMC3` ([Salvatier et al. 2016](#)), `radvel` ([Fulton et al. 2018](#)), `scipy` ([Jones et al. 2001](#)).

**Table 1.** Model Comparison.

| Description      | $N$ | $M$ | $N_{\text{data}}$ | $N_{\text{param}}$ | $\chi^2$ | $\chi^2_{\text{red}}$ | BIC    | $\Delta\text{BIC}$ |
|------------------|-----|-----|-------------------|--------------------|----------|-----------------------|--------|--------------------|
| Favored          | 2   | 2   | 2585              | 17                 | 3523.6   | 1.372                 | 3657.2 | 0.0                |
| Somewhat favored | 2   | 3   | 2585              | 19                 | 3512.7   | 1.369                 | 3662.0 | 4.8                |
| Disfavored       | 3   | 2   | 2585              | 19                 | 3543.1   | 1.381                 | 3692.4 | 35.2               |
| —                | 3   | 3   | 2585              | 21                 | 3536.8   | 1.379                 | 3701.9 | 44.6               |
| —                | 1   | 2   | 2585              | 15                 | 3680.0   | 1.432                 | 3797.9 | 140.7              |
| —                | 1   | 3   | 2585              | 17                 | 3670.2   | 1.429                 | 3803.8 | 146.6              |
| —                | 2   | 1   | 2585              | 15                 | 3700.9   | 1.440                 | 3818.8 | 161.6              |
| —                | 3   | 1   | 2585              | 17                 | 3710.2   | 1.445                 | 3843.7 | 186.5              |
| —                | 1   | 1   | 2585              | 13                 | 3872.7   | 1.506                 | 3974.8 | 317.6              |

NOTE— $N$  and  $M$  are the number of harmonics at the short and long periods, respectively.  $N_{\text{data}}$  is the number of fitted flux measurements.  $N_{\text{param}}$  is the number of free parameters in the model. The Bayesian information criterion (BIC) and the difference from the maximum  $\Delta\text{BIC}$  are also listed.

**Table 2.** Best-fit model priors and posteriors.

| Param.        | Prior                           | Mean      | Std. Dev. | 3%        | 97%       |
|---------------|---------------------------------|-----------|-----------|-----------|-----------|
| $P_s$         | $\mathcal{N}(0.4485; 0.0010)$   | 0.4484732 | 0.0000857 | 0.4483170 | 0.4486367 |
| $t_s^{(1)}$   | $\mathcal{N}(0.438096; 0.0020)$ | 0.4384733 | 0.0017440 | 0.4349337 | 0.4415021 |
| $R_p/R_*$     | $\mathcal{N}(0.1100; 0.0033)$   | 0.11      | 0.00308   | 0.10452   | 0.11599   |
| $b$           | $\mathcal{U}(0; 1 + R_p/R_*)$   | 0.7736    | 0.0756    | 0.6346    | 0.8993    |
| $u_1$         | (2)                             | 0.683     | 0.477     | 0.001     | 1.546     |
| $u_2$         | (2)                             | 0.004     | 0.417     | -0.793    | 0.727     |
| Mean          | $\mathcal{U}(-0.01; 0.01)$      | -0.000885 | 0.000440  | -0.001745 | -0.000088 |
| $\omega_s$    | $2\pi/P_s$                      | 14.01017  | 0.00268   | 14.00506  | 14.01505  |
| $A_{s,0}$     | $\mathcal{U}(-0.02; 0.02)$      | 0.008903  | 0.000705  | 0.007569  | 0.010277  |
| $B_{s,0}$     | $\mathcal{U}(-0.02; 0.02)$      | 0.009985  | 0.000751  | 0.008504  | 0.011289  |
| $A_{s,1}$     | $\mathcal{U}(-0.02; 0.02)$      | 0.001649  | 0.000696  | 0.000331  | 0.002884  |
| $B_{s,1}$     | $\mathcal{U}(-0.02; 0.02)$      | -0.005267 | 0.000606  | -0.006491 | -0.004203 |
| $\phi_\ell$   | $\mathcal{U}(1.3721; 2.1575)$   | 1.74324   | 0.22254   | 1.38274   | 2.08874   |
| $\omega_\ell$ | $\mathcal{N}(12.6054; 0.1261)$  | 12.588581 | 0.002040  | 12.584940 | 12.592450 |
| $A_{\ell,0}$  | $\mathcal{U}(-0.06; 0.06)$      | 0.037785  | 0.005150  | 0.028728  | 0.045214  |
| $B_{\ell,0}$  | $\mathcal{U}(-0.06; 0.06)$      | 0.022288  | 0.008592  | 0.008066  | 0.0359    |
| $A_{\ell,1}$  | $\mathcal{U}(-0.02; 0.02)$      | 0.002326  | 0.000756  | 0.000857  | 0.003658  |
| $B_{\ell,1}$  | $\mathcal{U}(-0.02; 0.02)$      | -0.002197 | 0.000744  | -0.003512 | -0.000743 |

(1) To convert mean TESS mid-transit time to  $\text{BJD}_{\text{TDB}}$ , add 2458468.2. (2) Quadratic limb-darkening prior from [Kipping \(2013\)](#), implemented by [Foreman-Mackey et al. \(2020\)](#).

## REFERENCES

- Agol, E., Luger, R., & Foreman-Mackey, D. 2019, [arXiv e-prints, 1908.03222](#)
- Astropy Collaboration, Price-Whelan, A. M., Sipőcz, B. M., et al. 2018, *AJ*, **156**, 123
- Barnes, J. W., van Eyken, J. C., Jackson, B. K., Ciardi, D. R., & Fortney, J. J. 2013, *The Astrophysical Journal*, **774**, 53
- Bhatti, W., Bouma, L. G., & Wallace, J. 2018, *astrobase*, <https://doi.org/10.5281/zenodo.1469822>
- Bouma, L. G., Hartman, J. D., Bhatti, W., Winn, J. N., & Bakos, G. Á. 2019, *ApJS*, **245**, 13
- Ciardi, D. R., Eyken, J. C. v., Barnes, J. W., et al. 2015, *The Astrophysical Journal*, **809**, 42, publisher: IOP Publishing
- Foreman-Mackey, D. 2016, *The Journal of Open Source Software*, **24**
- Foreman-Mackey, D., Czekala, I., Luger, R., et al. 2020, *exoplanet-dev/exoplanet v0.2.6*
- Fulton, B. J., Petigura, E. A., Blunt, S., & Sinukoff, E. 2018, *PASP*, **130**, 044504
- Gaia Collaboration, Brown, A. G. A., Vallenari, A., et al. 2018, *A&A*, **616**, A1
- Gelman, A., & Rubin, D. B. 1992, *Statistical Science*, **7**, 457, publisher: Institute of Mathematical Statistics
- Ginsburg, A., Sipocz, B., Madhura Parikh, et al. 2018, *Astropy/Astroquery: V0.3.7 Release*
- Hoffman, M. D., & Gelman, A. 2014, *Journal of Machine Learning Research*, **15**, 1593
- Howarth, I. D. 2016, *Monthly Notices of the Royal Astronomical Society*, **457**, 3769
- Hunter, J. D. 2007, *Computing in Science & Engineering*, **9**, 90
- Jenkins, J. M., Twicken, J. D., McCauliff, S., et al. 2016, *Software and Cyberinfrastructure for Astronomy IV*, 9913, 99133E
- Johns-Krull, C. M., Prato, L., McLane, J. N., et al. 2016, *The Astrophysical Journal*, **830**, 15
- Jones, E., Oliphant, T., Peterson, P., et al. 2001, *Open source scientific tools for Python*
- Kamiaka, S., Masuda, K., Xue, Y., et al. 2015, *Publications of the Astronomical Society of Japan*, **67**, 94
- Kipping, D. M. 2013, *mnras*, **435**, 2152
- Koen, C. 2015, *Monthly Notices of the Royal Astronomical Society*, **450**, 3991
- Kounkel, M., Covey, K., Suárez, G., et al. 2018, *The Astronomical Journal*, **156**, 84
- Lee, C.-H., & Chiang, P.-S. 2018, *The Astrophysical Journal Letters*, **852**, L24
- Lightcurve Collaboration, Cardoso, J. V. d. M., Hedges, C., et al. 2018, *Lightcurve: Kepler and TESS time series analysis in Python*, *Astrophysics Source Code Library*, [ascl:1812.013](#)
- Lomb, N. R. 1976, *Astrophysics and Space Science*, **39**, 447
- Luger, R., Agol, E., Foreman-Mackey, D., et al. 2019, *aj*, **157**, 64
- Luger, R., Bedell, M., Vanderspek, R., & Burke, C. J. 2019, [arXiv:1903.12182 \[astro-ph\]](#), *arXiv: 1903.12182*
- McKinney, W. 2010, in *Proceedings of the 9th Python in Science Conference*, ed. S. van der Walt & J. Millman, 51
- Onitsuka, M., Fukui, A., Narita, N., et al. 2017, *Publications of the Astronomical Society of Japan*, **69**
- Paxton, B., Bildsten, L., Dotter, A., et al. 2011, *ApJS*, **192**, 3
- Paxton, B., Cantiello, M., Arras, P., et al. 2013, *ApJS*, **208**, 4
- Paxton, B., Marchant, P., Schwab, J., et al. 2015, *ApJS*, **220**, 15
- Pérez, F., & Granger, B. E. 2007, *Computing in Science and Engineering*, **9**, 21
- Raetz, S., Schmidt, T. O. B., Czesla, S., et al. 2016, *Monthly Notices of the Royal Astronomical Society*, **460**, 2834
- Rebull, L. M., Stauffer, J. R., Cody, A. M., et al. 2020
- . 2018, *The Astronomical Journal*, **155**, 196
- Ricker, G. R., Winn, J. N., Vanderspek, R., et al. 2015, *Journal of Astronomical Telescopes, Instruments, and Systems*, **1**, 014003
- Salvatier, J., Wiecki, T. V., & Fonnesbeck, C. 2016, *PyMC3: Python probabilistic programming framework*
- Scargle, J. D. 1982, *The Astrophysical Journal*, **263**, 835
- Schmidt, T. O. B., Neuhauser, R., Briceño, C., et al. 2016, *Astronomy and Astrophysics*, **593**, A75
- Shporer, A. 2017, *PASP*, **129**, 072001
- Smith, J. C., Morris, R. L., Jenkins, J. M., et al. 2017a, *Kepler Science Document*, **7**
- Smith, J. C., Stumpe, M. C., Jenkins, J. M., et al. 2017b, *Kepler Science Document*, **8**
- Stassun, K. G., Oelkers, R. J., Pepper, J., et al. 2018, *AJ*, **156**, 102
- Stassun, K. G., Oelkers, R. J., Paegert, M., et al. 2019, [arXiv:1905.10694 \[astro-ph\]](#), *arXiv: 1905.10694*
- Stauffer, J., Rebull, L. M., Cody, A. M., et al. 2018, *The Astronomical Journal*, **156**, 275, publisher: American Astronomical Society
- Tanimoto, Y., Yamashita, T., Ui, T., et al. 2020, *PASJ*, [arXiv:2001.00148 \[astro-ph.EP\]](#)
- Tenenbaum, P., & Jenkins, J. 2018, *TESS Science Data Products Description Document*, EXP-TESS-ARC-ICD-0014 Rev D, <https://archive.stsci.edu/missions/tess/doc/EXP-TESS-ARC-ICD-TM-0014.pdf>
- Theano Development Team. 2016, *arXiv e-prints*, [abs/1605.02688](#)
- van Eyken, J. C., Ciardi, D. R., von Braun, K., et al. 2012, *The Astrophysical Journal*, **755**, 42
- VanderPlas, J. T., & Ivezić, Z. 2015, *The Astrophysical Journal*, **812**, 18
- Walt, S. v. d., Colbert, S. C., & Varoquaux, G. 2011, *Computing in Science & Engineering*, **13**, 22
- Yu, L., Winn, J. N., Gillon, M., et al. 2015, *The Astrophysical Journal*, **812**, 48